molecules

MDPI

Article

Influence of Processing Parameters on the Mechanical Properties of 3D Printed Borosilicate Particulate Reinforced Polymer Composites

Lucian Alexander-Roy [1], **Meelad Ranaiefar** [2], **Mrityunjay Singh**[3], **and Michael C. Halbig** [2*]

[1] Ohio Space Grant Consortium Intern, Case Western Reserve University, Cleveland, OH, 44106 USA
[2] NASA Glenn Research Center, Cleveland, OH, 44135 USA
[3] Ohio Aerospace Institute, Cleveland, OH, 44142 USA
* Correspondence: michael.c.halbig@nasa.gov

Abstract

Emerging composite materials are expanding the potential of additive manufacturing and enabling applications previously restricted by traditional manufacturing methods. The multi-phase nature of these composite materials combined with the complex internal geometry of additively manufactured parts have enabled unique behavior, and potentially new applications. Additionally, these materials can be pyrolyzed to create dense metal, ceramic, and glass parts with geometries typically not achievable by traditional processes. Additive manufacturing of borosilicate glass-based systems can open new applications in nuclear engineering, astronomy, and bone regrowth therapy. To elucidate the process-parameter relationship of borosilicate-polylactic acid (PLA) composites, mechanical testing was conducted and compared with a pure polylactic acid polymer baseline. Test specimens were fabricated by fused-filament fabrication with minimal post-processing. Yield strength, ultimate strength, and elastic modulus were calculated from stress-strain curves. Optical and scanning electron microscopy were conducted to observe the specimen microstructure before and after testing. The highest compressive yield strength for the composite was 28.22 MPa, and the highest compressive yield strength for PLA was 49.30 MPa. Print orientation was found to benefit the composite material but have a detrimental effect on the pure matrix material. An elastic modulus of 2.66 GPa was recorded for the borosilicate-PLA composite at 100% infill, 1 shell wall, and layer lines parallel to compression axis. Microscopy revealed that lower modulus composite specimens had the particulates re-distributed within the matrix. Tensile testing was done according to a polymer testing standard, which caused difficulties obtaining consistent fracture within the gauge length.

Keywords: 3D Printing, composites, borosilicate, PLA, mechanical testing

Academic Editor: Firstname Lastname

Received: date
Revised: date
Accepted: date
Published: date

Citation: To be added by editorial staff during production.

1. Introduction

Since the invention of the first borosilicate glass in the early 1880s by Otto Schott, its uses have become widespread and increased manyfold around the globe. The main advantage provided by borosilicate glasses is their extremely low coefficient of thermal expansion (CTE) compared with traditional glasses. Alkali or alkaline earth network modifiers are added to a borate (B_2O_3) network in precise concentrations to reduce CTE and increase the glass transition temperature [1]. Borosilicate glasses are common in laboratory and household kitchen use for their resistance to thermal shock and chemical corrosion. They also serve a critical role in telescope mirrors to minimize image distortions due to thermal expansion of the mirrors [2]. The durability and radiation resistance of borosilicate glasses made it the primary solvent for immobilization of high-level nuclear waste materials [3-4]. Additionally, borosilicate glasses have been shown to have potential in the field as bioactive materials, particularly for promoting regeneration of bone [5-6]. Such varied applications mean any advancements in the manufacture of borosilicate glass have the potential to have widespread impact.

Some of the most prominent advancements in manufacturing technology in the past decades have been in the field of additive manufacturing (AM). One of the most widespread AM approaches uses thermoplastic feedstock in a fused-filament fabrication (FFF) process. This process produces near-net shape polymer parts by pushing filament or pellets through a heated nozzle in a computer-controlled toolpath, with minimal or no post processing needed. One of the most common materials for FFF is polylactic acid (PLA). PLA is derived from corn starch, and does not require enzymes to catalyze its reaction, making it easy to manufacture. In addition to its biocompatibility and compostability, the composite offers tailorable crystallinity, allowing it to be processed into either amorphous or crystalline structures [7]. The material capabilities of FFF are expanded through use of composites and secondary processing techniques. By loading a thermoplastic with metal, ceramic, or glass particulates, green body parts can be printed by traditional FFF methods, processed to remove the thermoplastic matrix, then sintered in a furnace to densify the particulates into a solid part. Compared with other methods for AM of ceramics and metals like selective laser sintering or binder jetting, FFF has significantly lower barriers to entry in terms of equipment cost and complexity. The uniform heating of the secondary sintering process results in a more isotropic material compared with selective laser sintering, which can be prone to columnar grain growth [8]. Additionally, these composite materials may have other uses beyond AM. Particle reinforcement is commonly used to improve the mechanical and tribological properties of polymers and other matrix materials [9-10]. Inorganic nanoparticle-polymer composites are utilized in bioimaging, photovoltaics, and various other fields [11]. It is worthwhile to explore novel borosilicate composites and manufacturing processes, considering their numerous applications.

To enable the use of these novel materials in large-scale manufacturing, properties such as material strength, wear resistance, and density must be understood. Additional factors are introduced by the 3D printing process; the user's slicing parameters determine the geometry of the toolpath, and these settings can affect the mechanical characteristics of the finished product. For example, reduction in infill percentage can provide critical material savings and faster print times, however this can come with a tradeoff in reduced mechanical strength. Certain printing orientations are necessary to print parts with large overhangs but can cause undesirable weakness to shear forces along layer lines. With the introduction of secondary particulate phases, interactions between the matrix, dispersion, and print geometry become even more complex. This report explores the effect of print parameter settings on the mechanical behavior of a composite filament made of borosilicate glass and PLA (BSC-PLA). Compression and tensile tests of as-printed test specimens of BSC-PLA and pure PLA were conducted to compare mechanical properties. Visual and statistical analysis were applied to observe the effects of varying print parameters on qualitative properties.

2. Results and Discussion

As shown in **Table 1** and **Table 2**, the pure PLA is significantly stronger than BSC-PLA in compression. For 100% infill compression specimens, the Young's moduli are similar but slightly reduced between the PLA to the BSC-PLA, but close to the accepted values for pure PLA [12]. Infill % was the strongest factor in determining compressive yield strength in BSC-PLA samples. The design of experiments (DoE) revealed that, in addition to increased infill percent, fewer walls had a positive effect on the yield strength as well as the elastic modulus. Furthermore,-the composite material's yield strength and modulus benefits from the 90° print orientation. This contrasts with the pure PLA data, which sees decreased strength from both parameters. The BSC-PLA samples exceeded the PLA sample's elastic modulus in both 50% and 100% infill samples with 1 shell and 90° print orientation. This increase in stiffness suggests that the borosilicate particles are playing a more active role in compression with these parameters.

Table 1. PLA batch parameters and compression response values. All batches were printed with a 0.2 mm print layer height.

Batch #	Infill %	Shells	Orientation [°]	σ_{yield} [MPa]	E [GPa]
1	50	1	0	23.2 ± 0.60	1.15 ± 0.05
2	50	1	90	21.0 ± 1.20	1.03 ± 0.04
3	50	3	0	37.5 ± 1.04	1.72 ± 0.04
4	50	3	90	29.1 ± 0.46	1.45 ± 0.03
5	100	1	0	62.2 ± 2.60	2.61 ± 0.12
6	100	1	90	47.6 ± 0.86	2.45 ± 0.06
7	100	3	0	63.1 ± 1.59	2.58 ± 0.07
8	100	3	90	49.3 ± 0.35	2.48 ± 0.04

Table 2. BSC-PLA batch parameters and compression response values. All batches were printed with a 0.2 mm print layer height.

Batch #	Infill %	Shells	Orientation [°]	σ_{yield} [MPa]	$\sigma_{ultimate}$ [MPa]	E [GPa]
1	50	1	0	9.65 ± 0.20	19.47 ± 0.14	1.01 ± 0.06
2	50	1	90	9.65 ± 0.20	13.29 ± 0.54	1.04 ± 0.15
3	50	3	0	9.65 ± 0.20	14.08 ± 7.04	0.7 ± 0.09
4	50	3	90	10.42 ± 0.44	9.78 ± 0.14	0.75 ± 0.05
5	100	1	0	7.15 ± 0.17	36.85 ± 0.69	2.07 ± 0.19
6	100	1	90	7.36 ± 0.12	34.35 ± 0.84	2.66 ± 0.23
7	100	3	0	21.63 ± 1.06	30.01 ± 0.48	1.55 ± 0.09
8	100	3	90	28.22 ± 0.61	21.13 ± 10.57	1.82 ± 0.29

The Pareto chart in **Figure 1** summarizes the relative effects of the printing parameters and their interactions on the compressive yield strength of BSC-PLA specimens. The t-value represents the statistical magnitude of each factor's contribution to the response, while the sign indicates whether the effect is positive or negative. Infill percentage (C) exhibited the largest positive effect by a substantial margin, indicating that increasing infill from 50% to 100% was the dominant factor controlling compressive yield strength. This behavior is consistent with the reduction in internal porosity and the corresponding increase in load-bearing material. Shell count (B) was the second most influential factor and exhibited a negative effect on yield strength. Additionally, the significant shell–infill interaction (B×C) indicates that the influence of shell count in part depends on the selected infill level. Print orientation (A) also had a significant positive effect, with the 90° orientation generally producing higher yield strengths than the 0° orientation, suggesting that the alignment of deposited tracks influences stress transfer during compression. The A×C interaction was also statistically significant, indicating that the influence of orientation becomes more pronounced as infill percentage increases. By contrast, the A×B interaction had only a minor contribution, and the three-factor interaction (A×B×C) did not exceed the significance threshold and was therefore excluded from further consideration. Overall, the results demonstrate that compressive yield strength in BSC-PLA is governed primarily by infill percentage, with shell count and print orientation exerting important secondary effects and interactions.

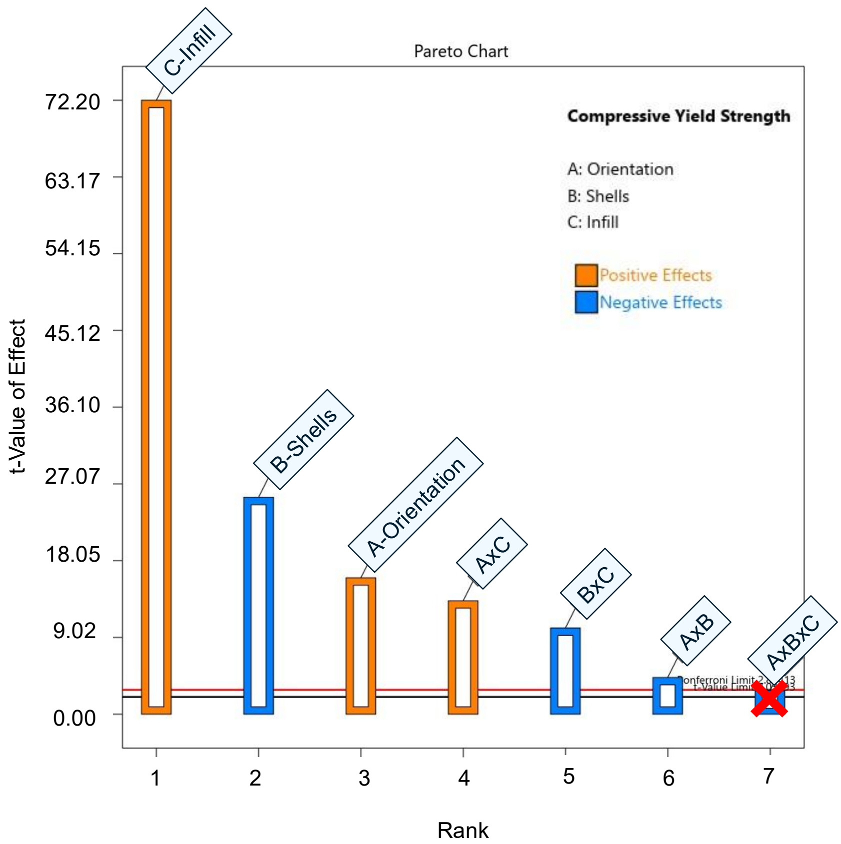

Figure 1. BSC-PLA yield strength vs print parameter effects and interactions. The AxBxC interaction is below the significance criteria and has been marked with a red "X".

Mechanical testing revealed that macroscopic failure modes were highly dependent on the selected print parameters. Specimens printed with 50% infill frequently exhibited perimeter wall buckling and subsequent delamination from the internal infill structure. Additionally, distinct diagonal shear bands were observed in samples printed with a 0° orientation. **Figure 2** illustrates the contrast in deformation behavior between a 50% infill, 3-shell specimen printed at 0° (**Figure 2a**) and a 50% infill, 1-shell specimen printed at 90° (**Figure 2b**). Notably, the 0° orientation samples sustained higher strain values prior to failure, whereas single-wall specimens were particularly susceptible to diagonal shearing.

(a)

(b)

Figure 2. Post-test compression samples: (a) Compression batch 3; (b) Compression batch 2.

Digital image correlation (DIC) analysis provided further insight into these underlying deformation mechanisms. As shown in the DIC strain map of a BSC-PLA Batch 2 specimen (**Figure 3**), captured just prior to reaching ultimate compressive load, localized strain concentrations are clearly visible. The teal bands stretching across the specimen surface indicate regions where internal voids within the infill matrix collapsed prematurely compared to the surrounding exterior shells, leading to uneven stress distribution and eventual failure.

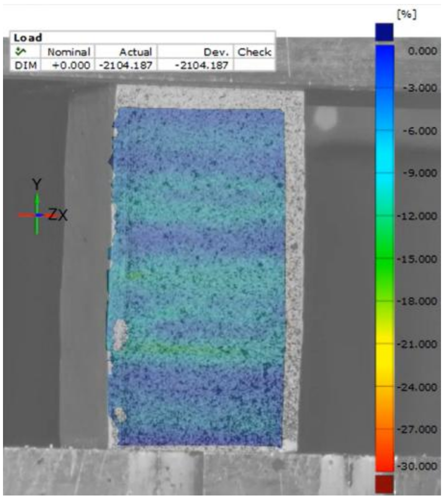

Figure 3. DIC strain map of BSC-PLA batch 2.

Microstructural analysis provided insight into the distribution of the borosilicate particulates within the PLA matrix (**Figure 4**). The particles exhibited a predominantly spherical morphology, with diameters ranging from 10 μm to over 100 μm observed in the optical micrographs. Notably, minimal voids were detected at the interface between the PLA matrix and the glass particles, indicating adequate wetting of the filler material in the as-printed state. Furthermore, analysis of the post-compression specimens revealed distinct fracturing of the glass particulates, highlighting their active engagement in the material's stress response and subsequent failure.

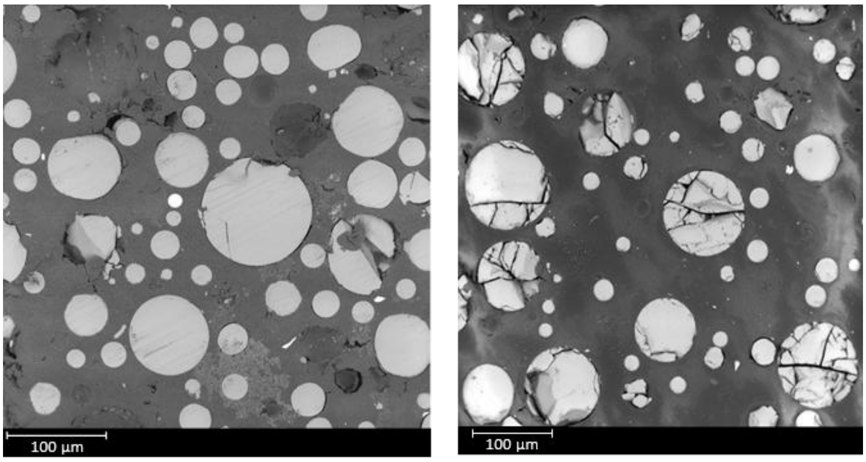

(a) **(b)**

Figure 4. SEM microscopy of BSC-PLA. (a) 620x magnification pre-compression; (b) 520x magnification post-compression.

A larger-scale overview of the particle distribution within the samples can be seen in **Figure 5**. Images were selected of samples with the highest and lowest elastic modulus for 100% infill. The samples were mounted to view along the axis of compression. In the high elastic modulus sample (Batch 6), we see uniform distribution of the glass particles within the matrix. However, in the low elastic modulus sample (Batch 7), there are clear regions where the particles have become concentrated, visible both along the compression axis and on the compression plane. A similar trend is noted in the 50% infill samples, but the effect is less apparent, possibly because these tend to fail due to stress concentrations caused by voids in the infill pattern before failing due to material strength limits. The particle distribution within the matrix for uncompressed samples is homogenous.

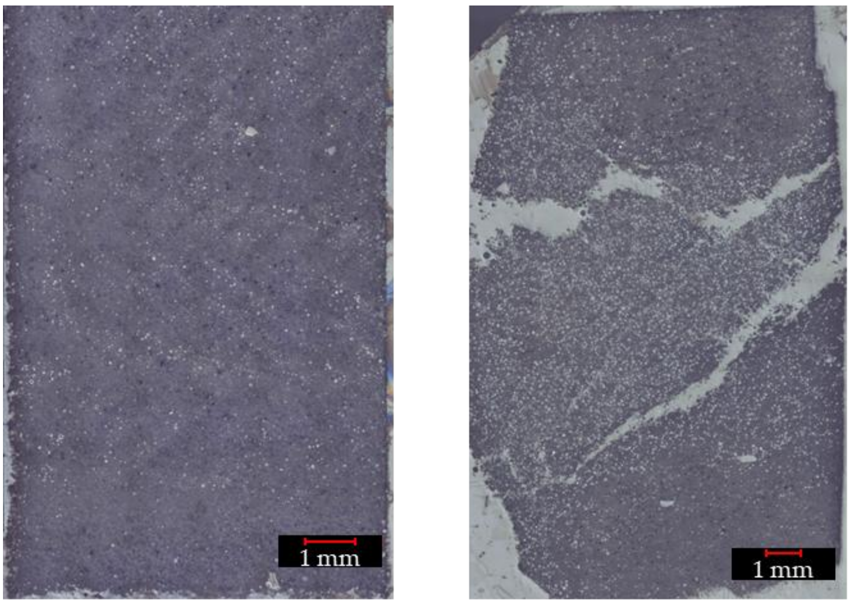

(a) **(b)**

Figure 5. Optical microscopy of post-compression BSC-PLA. Darker regions are PLA, lighter speckles are borosilicate: **(a)** Batch 6 compression axis; **(b)** Batch 7 compression axis.

In other literature studies, similar compression tests on epoxy-glass particulate composites were conducted. Pre- and post-test microscopy from Singh et al. shows that the 34 μm glass beads embedded in epoxy matrix were not fractured after dynamic compression testing [13], unlike the damage noted in our SEM images. Elastic modulus was measured by Bhatia et al. for a 70 wt. %-epoxy, 30 wt. %-glass mixture, with E values of 1.57 GPa for spherical particles in the size range of 20 μm and 50 μm [14], which is lower but comparable to the results of this work. Cho et al. tested a distribution of glass particle sizes within vinyl resin epoxy and found that the elastic modulus of the composite increased with decreasing particle size in the nanoscale range but was unaffected by particles on the micron level [15]. The literature review returned no works which utilize additively manufactured glass-PLA specimens.

Having contrasted the BSC-PLA's modulus against pure PLA and other similar composite materials, we can also compare the results with models which attempt to predict the effective modulus of a composite system. The simplest model, known as the Reuss model, describes the lower bound of the elastic modulus for a composite material under iso-stress conditions (applicable to particulates dispersed in matrix), given by Equation 1 [16].

$$E_{eff} = \frac{E_m E_d}{f E_m + (1-f) E_d} \tag{1}$$

Where E_{eff} is the effective elastic modulus of the composite, E_m is the elastic modulus of the matrix, E_d is the elastic modulus of the dispersion, and f is the volume fraction of the dispersion. ImageJ analysis of 3 sample images was used to calculate the area fraction of particulates given in **Table 3.** Typical area fraction measurements in isotropic regions of the material had consistent values between 30-35%.

Table 3. Borosilicate particle area fraction measurements. Images available in Appendix A.

Image Filename	Area %
BSC7C0001.tiff	34.49
BSC80006.tiff	33.56
BSC80002.tiff	29.80

Later work by Yunhua Luo provides a more complex model which accounts for elasticity relations and the Poisson effect [17]. For iso-stress condition, given by Equation 2:

$$E_{eff} = \frac{E_m E_d [f E_m (1-\nu_d) + E_d (1-f)(1-\nu_m)]}{\begin{gathered} E_m E_d [\nu_m (1-f)^2 (1-\nu_d) + \nu_d f^2 (1-\nu_m)] + \\ f(1-f) {E_m}^2 [(1+\nu_d)(1-2\nu_d)] + 4\nu_d \nu_m E_d E_m + (1+\nu_m)(1-2\nu_m) E_d^2 \end{gathered}} \tag{2}$$

Where ν_m is the Poisson's ratio of the matrix material and ν_d is the Poisson's ratio for the dispersed particles. Material properties for the constituent materials were taken from current literature to compare calculated elastic modulus values with the observed values. The volume fraction was taken from the average of the ImageJ analysis results. Poisson's ratio values for PLA and borosilicate are well defined, as are elastic modulus values for PLA. For PLA, the elastic modulus was taken as 2.54 GPa [12]. The Poisson's ratios were taken as 0.36 and 0.22 for PLA and borosilicate, respectively [18, 19]. Since the exact composition of the borosilicate in BSC-PLA is unknown, each of the models was compared using multiple borosilicate modulus values from A. Abd El-Moneim [20], and the results are shown in **Table 4.**

Table 4. Predicted effective modulus of BSC-PLA.

Borosilicate Elastic Modulus [GPa]		35.65	45.63	67.65
Effective Modulus [GPa]	Reuss Model	6.79	6.98	7.23
	Luo Model	5.08	5.24	5.46

Luo's improved Reuss model predicts the closest values to our observed effective elastic moduli, but all models fall outside the range seen in Table 2. Since our observed PLA elastic modulus values are similar to the accepted values from the literature (2.45-2.61 GPa) [12], it is unlikely that the modulus differences are due to the 3D printing geometry. If particle-matrix interface adhesion is particularly poor compared to typical composites, this could lead to reduced load transfer, resulting in lower-than-expected elastic modulus values.

Tensile tests were also conducted for both BSC-PLA and PLA, with 100% infill percentage and additional print details of infill angle, number of shells, and layer height provided in **Table 5**. However, difficulties arose in obtaining consistent breakage/deformation within the gauge length of the BSC-PLA specimens. The material behaves with much less ductility in this test condition compared with compression, causing many samples to break prematurely or at/near the test stand grips. This is a well-known difficulty with tensile testing of brittle materials like ceramics or glasses [21]. For this reason, the quality of the tensile response values for elastic modulus, yield and ultimate strength are called into question. The 0° tensile samples tended to break outside the gauge length more than the 90° samples (**Figure 6**) and had much smoother fracture surfaces due to delamination at the layer lines.

Table 5. Tensile testing details of experimental batches with 100% infill.

Batch #	**Infill Angle**	**Shells**	**Layer Height**
1	0	5	0.3
2	0	1	0.3
3	90	5	0.3
4	90	1	0.3
5	45	3	0.2
6	0	5	0.1
7	0	1	0.1
8	90	5	0.1
9	90	1	0.1

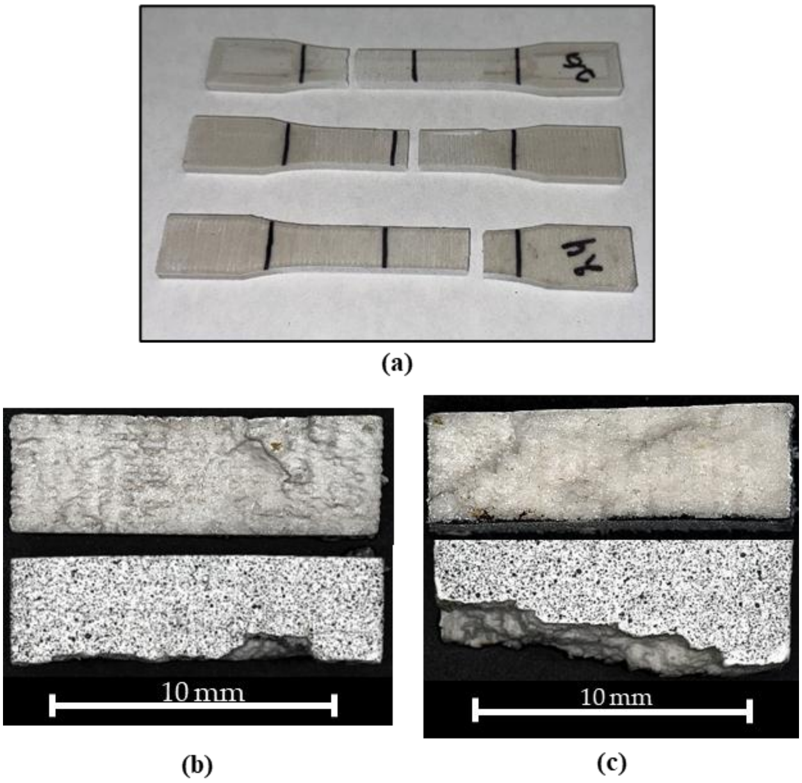

Figure 6. (a) Tensile samples with varying failure modes. The top sample (90° infill) has a rough fracture surface near the grip. The middle sample (0° infill) has a clean break near the center of the gauge length. The bottom sample (0° infill) has a rough break at the grips; (b) Batch 3 fracture surface and profile; (c) Batch 7 fracture surface and profile

3. Materials and Methods

3.1 Specimen Preparation

A Design of Experiments (DoE) approach was implemented to investigate how various printing parameters influence mechanical behavior under compression and tension. In AM, there are many key parameters to be considered include infill percentage, infill pattern, number of outer walls (or shells), layer height, and the build orientation relative to the applied load (i.e., parallel or perpendicular to the layers) [22–25]. The DoE methodology allows for systematic variation of several factors simultaneously while minimizing the total number of required tests. This strategy has been widely adopted in other studies involving multiple additive manufacturing parameters [23].

Compression testing of the PLA and BSC-PLA specimens was carried out using three selected print parameters, each evaluated at two levels: number of shells (1|3), infill percentage (50%|100%), and layer orientation (0°|90°). Orientation refers to the angle of the printed layers relative to the loading direction, where 0° indicates layers are aligned perpendicular to the compression axis, and 90° corresponds to layers oriented parallel to it (see **Figure 7a**). A full factorial DoE was employed, resulting in eight unique parameter combinations across the specimen batches. Batch identifiers and corresponding print settings are provided in **Section 2 Tables 1-2**.

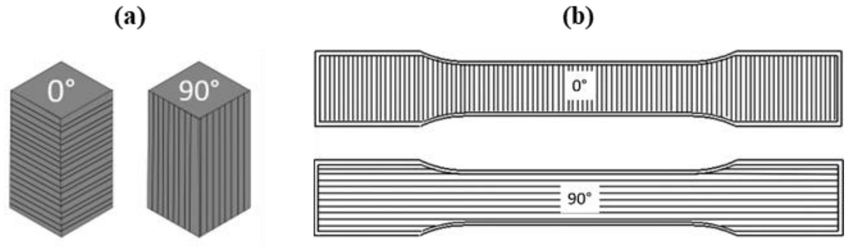

Figure 7. Layer dependence on orientation. (a) Compression specimen, (b) Tensile specimen. Reproduced from [26].

Although, layer height is known to influence strength due to printing anisotropy, it was held constant at 0.2 mm to minimize its effect and isolate the impact of other parameters. While infill patterns ranging from simple grid layouts to complex gyroid structures can have significant impact on strength, it was not varied in this study. A consistent honeycomb infill was chosen to simplify the DoE, as quantifying complex infill geometry in this context is challenging. Investigations into infill pattern effects are better addressed in dedicated studies such as those by Birosz et al. and Dudescu et al. [22, 25]. By focusing on a limited set of variables, the study maintains a manageable experimental scope while preserving the statistical strength and reliability of the resulting insights.

For the tensile testing DoE, three parameters were evaluated at two levels with an additional midpoint selected: number of shells (1|3|5), infill orientation (0|45|90°), and layer height (0.1|0.2|0.3mm). In this context, orientation refers to the direction of the rectilinear infill pattern within the solid regions; shell geometry remains consistent across orientations. Additionally, all tensile specimens were printed with solid infill, as the thin geometry of standard dog-bone samples does not allow for meaningful variation in infill volume [27]. Batch identifiers and their associated print parameters are listed in **Section 2 Table 5.**

Compression specimens were designed in SolidWorks 2024 (Dassault Systèmes, Vélizy-Villacoublay, FR) based on ASTM D695 [28], using a rectangular prism geometry with dimensions of 12.7 mm × 12.7 mm × 25.4 mm (**Figure 8a**). A rectangular shape was selected instead of a cylindrical form due to anticipated difficulties when printing curved geometries at a 90° orientation. The model was exported as an STL file for 3D printing.

Tensile specimens were modeled according to ASTM D638 [29], with dimensions shown in **Figure 8b**. A thickness of 4.2 mm was chosen to allow consistent printing at multiple layer heights. Nine batches, each containing three specimens, were printed for tensile testing, resulting in 27 specimens per material.

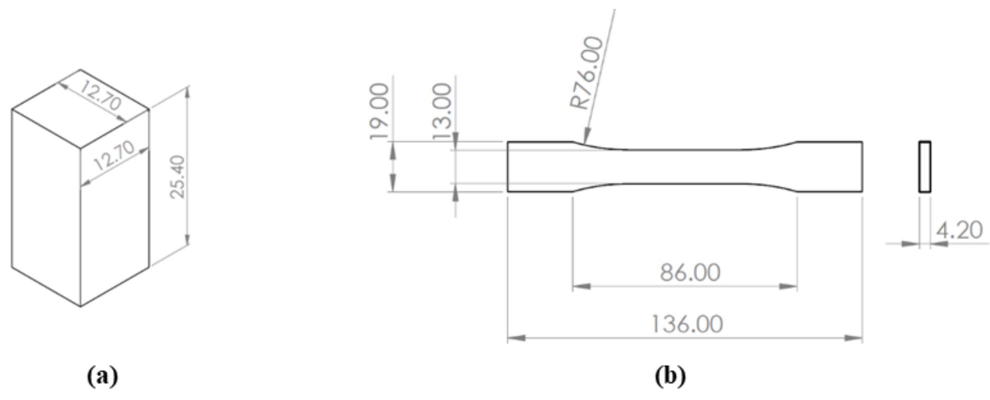

Figure 8. Test specimen dimensions, in mm. (a) Compression test specimen dimensions; (b) Tensile test specimen dimensions. Reproduced from [26].

Two materials in the form of filament were evaluated: a borosilicate-filled PLA composite (BSC-PLA) from The Virtual Foundry (Stoughton, WI), and a standard PLA from Raise3D (Irvine, CA), both with a nominal diameter of 1.75 mm. The composition of BSC-PLA is provided in **Table 6**.

Table 6. Borosilicate filament composition (data provided by The Virtual Foundry).

Material	% wt.
Borosilicate	68.65-70.65
Binding Additive	-
PLA	<31.00

Slicing was performed using ideaMaker 4.3.1 (Raise3D), and specimens were printed on a Raise3D Pro3 at a speed of 60 mm/s. BSC-PLA prints were carried out at 220 °C using a 0.8 mm steel nozzle, while PLA was printed at 205 °C with a 0.6 mm brass nozzle, following manufacturer recommendations. For compression specimens, minimal surface sanding using #3/0 grit sandpaper was applied to the end faces to ensure level contact with the testing apparatus and to reduce localized stress concentrations. Otherwise, specimens were tested in their as-printed state. For specimens used in digital image correlation (DIC), the gauge region was coated with white paint and overlaid with a black speckle pattern to enable surface strain mapping.

Samples were sectioned, mounted, and polished for microscopic analysis. Specimens were selected from both pre- and post-compression batches. Cuts were made parallel and perpendicular to the printed layer lines using a Techcut 5 precision saw (Allied High-Tech Products, Compton, CA, USA), and then mounted in two-part epoxy (Metlab Corporation, Niagara Falls, NY, USA). For 50% infill specimens, air was evacuated in a vacuum chamber during curing to ensure complete epoxy infiltration. Mounted samples were ground approximately 3 mm to eliminate surface contamination and cutting debris. Polishing was performed in successive stages on a Struers Abrapol-30 (Copenhagen, DK) using diamond suspensions with decreasing grit sizes of 9 μm, 6 μm, 3 μm, and 1 μm.

3.2 Testing

Compression tests were performed using an Instron 8562 universal testing machine. Prior to testing, each specimen's mass and dimensions (length, width, and height) were recorded. Testing followed the ASTM D695 standard, utilizing a compression speed of 1.3 mm/min and a maximum displacement limit of 13 mm. Load and position data were captured at a sampling rate of 10 Hz, with peak load values manually recorded from the machine interface. In most cases, tests were terminated before reaching the displacement limit due to significant specimen deformation.

Tensile tests were conducted on an Instron 5966 machine. As with compression testing, specimen mass and cross-sectional area at the gauge section were measured beforehand. A mechanical extensometer (MTS, Eden Prairie, MN, USA) was employed to measure the change in length across the gauge section for strain calculations. Testing adhered to ASTM D638 guidelines, using a constant extension rate of 5 mm/min until failure.

3.3 Visual Analysis

Additional tension and compression tests were carried out using digital image correlation (DIC) via an ARAMIS system (Trilion Quality Systems, Plymouth Meeting, PA, USA). A virtual extensometer was used to generate load–strain plots synchronized with video recordings of the strain fields. Imaging was performed at 2 Hz during the initial 100 stages to capture high-resolution data throughout the elastic region, and then reduced to 0.25 Hz beyond the yield point to observe post-yield deformation behavior.

Microscopic analysis was conducted using a Phenom ProX desktop scanning electron microscope (Thermo-Fisher, Waltham, MA, USA) and a Keyence VHX-7000 optical microscope. Both pre- and post-compression specimens were examined to identify microstructural changes resulting from compressive loading. SEM imaging was primarily performed using 15 kV intensity in image mode, with a full backscattered electron (BSD Full) detector. The volume fraction of borosilicate particles observed in the SEM micrographs was quantified using ImageJ software. For optical microscopy, large-area images of the specimen surface were created using the stitching function to combine multiple fields of view, allowing for evaluation of particle dispersion and morphology within the PLA matrix.

3.4 Statistical Analysis

Stress–strain curves were generated using Python and Matplotlib, based on load, displacement, and specimen dimension data collected during mechanical testing. For each specimen, individual plots were created that included calculations of Young's modulus and yield strength, determined from the slope of the linear elastic region. A standard 0.002 strain offset method was applied to estimate the yield point (**Figure 9**). Mean and standard deviation values for yield strength, ultimate tensile strength, and elastic modulus were computed in Excel for both PLA and BSC-PLA batches and reported in **Table 1** and **Table 2.**

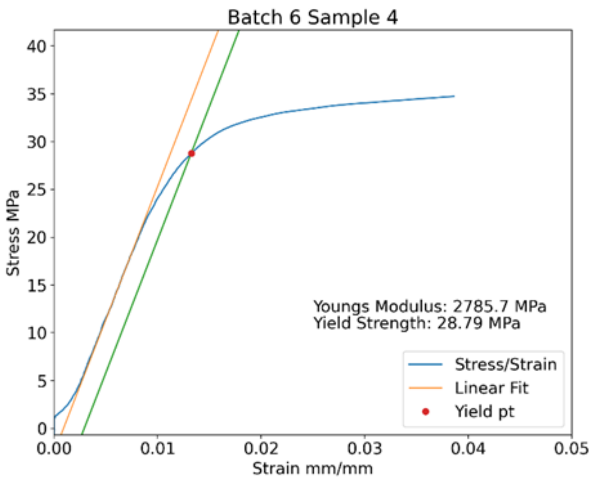

Figure 9. Example compression stress-strain curve of one sample with 100% infill, 1 shell, 90° orientation

Statistical analysis of mechanical properties was performed using Design-Expert (StatEase, Minneapolis, MN, USA) to assess the influence of each parameter and their interactions. P-values for the responses are included in Appendix B. The R-squared plot indicated that the model accounted for all data points within the acceptance criteria (see Appendix C).

4. Conclusions

Borosilicate glass's unique thermal, chemical, and structural properties make it a highly useful material for a myriad of industries, including laboratory settings, telescopes, nuclear power, and biomedical engineering. Developments in additive manufacturing have made 3D printing borosilicate glass more accessible than ever through new composite materials. However, the effect of print parameters on the behavior of these composites is not well understood. This work explores the mechanical properties of borosilicate glass-PLA composite test specimens created by fused-filament fabrication using varying print parameters. A design of experiments was utilized to elucidate the strength of varying factors and their interactions on yield strength, ultimate strength, and elastic modulus. The standard PLA had higher yield and ultimate strength in all cases, but certain print configurations granted higher elastic modulus for the borosilicate-PLA composite. Microscopy showed that the lowest elastic modulus samples had non-homogeneous particulate dispersions post-compression, indicating independent motion of the phases during loading. Tensile testing was done according to a polymer testing standard, which caused difficulties obtaining consistent fracture within the gauge length. Future works should consider using a ceramic-based tensile test standard.

Author Contributions: Conceptualization, M.S., M.H. and M.R.; methodology, L.A.-R. and M.R.; software, L.A.-R.; validation, L.A.-R.; formal analysis, L.A.-R.; investigation, L.A.-R.; resources, M.H., M.S. and M.R.; data curation, L.A.-R.; writing—original draft preparation, L.A.-R.; writing—review and editing, L.A.-R., M.H., M.R. and M.S.; visualization, L.A.-R.; supervision, M.R., M.S. and M.H.; project administration, M.S. and M.H.; funding acquisition, M.S. and M.H. All authors have read and agreed to the published version of the manuscript.

Funding: This research was funded by the NASA Ohio Space Grant Consortium (OSGC) managed by Ohio Aerospace Institute.

Institutional Review Board Statement: Not applicable.

Informed Consent Statement: Not applicable.

Data Availability Statement: The raw data supporting the conclusions of this article will be made available by the authors on request.

Acknowledgments: The authors would like to thank the Ohio Space Grant Consortium, Jonathan Salem, Dan Gorican, Andrew Ring, and Dan Schieman for supporting this work.

Conflicts of Interest: The authors declare no conflicts of interest.

Abbreviations

The following abbreviations are used in this manuscript:

ASTM	American Society for Testing and Materials
BSC	Borosilicate
DoE	Design of Experiments
PLA	Polylactic Acid
SEM	Scanning Electron Microscopy

Appendix A 398

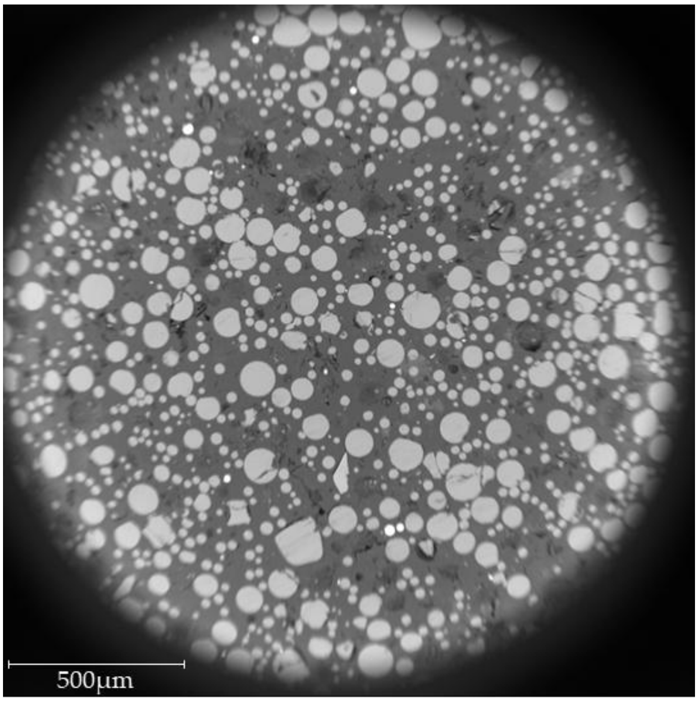

Figure A1. SEM for borosilicate particle area fraction measurement, BSC80006.tiff

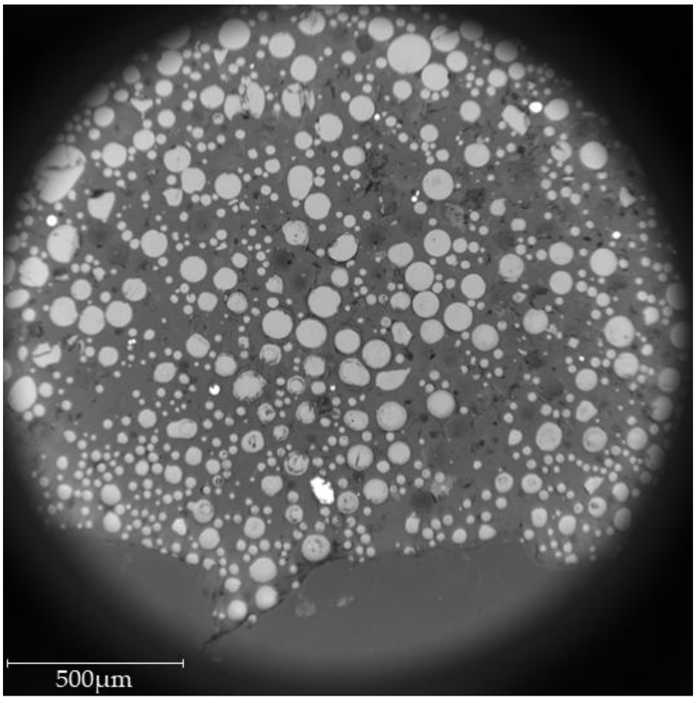

Figure A2. SEM for borosilicate particle area fraction measurement, BSC80002.tiff.

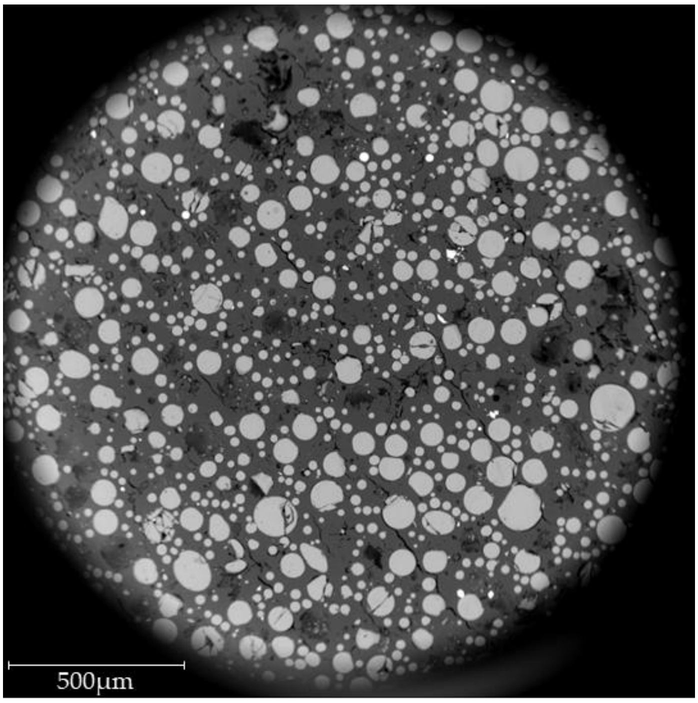

Figure A3. SEM for borosilicate particle area fraction measurement, BSC7C0001.tiff

Appendix B

Table B1. BSC-PLA factor p-values for compression tests.

	Yield Strength	Ultimate Strength	Young's Modulus
Model	<0.0001	<0.0001	<0.0001
A - Orientation	<0.0001	<0.0001	0.0004
B - Shells	<0.0001	<0.0001	<0.0001
C- Infill	<0.0001	<0.0001	<0.0001
AxB	0.0001	0.0005	0.0022
AxC	<0.0001	<0.0001	-
BxC	<0.0001	<0.0001	0.0032
AxBxC	0.0093	-	-

Table B2. PLA factor p-values for compression tests. Reproduced from [26].

	Yield Strength	Young's Modulus
Model	0.04	0.06
A - Orientation	0.29	0.34
B - Shells	-	-
C- Infill	0.51	0.31
AxB	-	-
AxC	0.01	0.02
BxC	-	-
AxBxC	-	-

Appendix C

Figure C1. BSC-PLA yield strength model vs data. The color gradient indicates lowest (blue) to highest (red) experimental value.

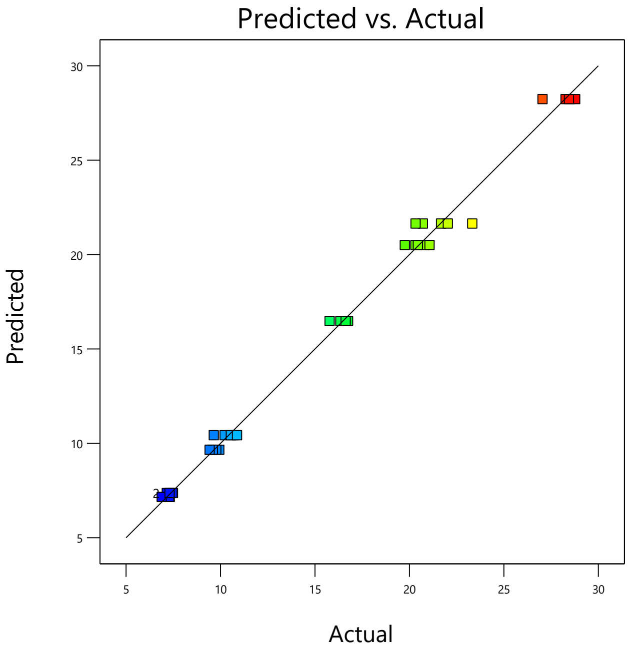

Figure C2. BSC-PLA elastic modulus model vs data. The color gradient indicates lowest (blue) to highest (red) experimental value.

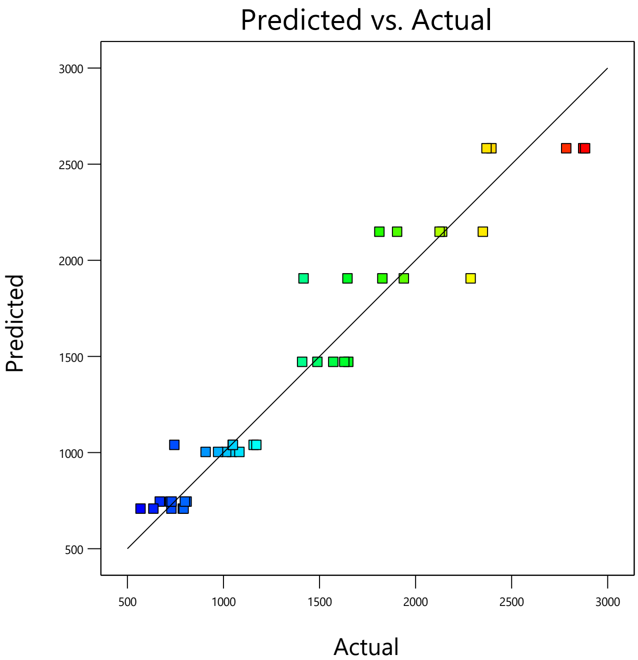

References

1. Uhlmann, D.R.; Shaw, R.R. The Thermal Expansion of Alkali Borate Glasses and the Boric Oxide Anomaly. Journal of Non-Crystalline Solids 1969, 1, 347–359, doi:10.1016/0022-3093(69)90018-0.
2. Matthews, G.W.; Whitman, T.L.; Feinberg, L.D.; Voyton, M.F.; Lander, J.A.; Keski-Kuha, R. JWST Telescope Integration and Test Progress.; MacEwen, H.A., Fazio, G.G., Lystrup, M., Batalha, N., Siegler, N., Tong, E.C., Eds.; Edinburgh, United Kingdom, July 29 2016; p. 990404.

3. Ringwood, A.E.; Kesson, S.E.; Ware, N.G.; Hibberson, W.; Major, A. Immobilisation of High Level Nuclear Reactor Wastes in SYNROC. Nature 1979, 278, 219–223, doi:10.1038/278219a0.
4. Plodinec, J. Borosilicate Glasses for Nuclear Waste Immobilization. Glass Technology - European Journal of Glass Science and Technology Part A 2000, 41, 186–192.
5. Rahaman, M.N.; Day, D.E.; Sonny Bal, B.; Fu, Q.; Jung, S.B.; Bonewald, L.F.; Tomsia, A.P. Bioactive Glass in Tissue Engineering. Acta Biomaterialia 2011, 7, 2355–2373, doi:10.1016/j.actbio.2011.03.016.
6. Kaur, G.; Pandey, O.P.; Singh, K.; Homa, D.; Scott, B.; Pickrell, G. A Review of Bioactive Glasses: Their Structure, Properties, Fabrication and Apatite Formation. J. Biomed. Mater. Res. 2014, 102, 254–274, doi:10.1002/jbm.a.34690.
7. Biopolymers from Renewable Resources; Kaplan, D.L., Ed.; Macromolecular systems - materials approach; Softcover version of original hardcover edition 1998.; Springer: Berlin, 2010; ISBN 9783642083419.
8. Grossin, D.; Montón, A.; Navarrete-Segado, P.; Özmen, E.; Urruth, G.; Maury, F.; Maury, D.; Frances, C.; Tourbin, M.; Lenormand, P.; et al. A Review of Additive Manufacturing of Ceramics by Powder Bed Selective Laser Processing (Sintering / Melting): Calcium Phosphate, Silicon Carbide, Zirconia, Alumina, and Their Composites. Open Ceramics 2021, 5, 100073, doi:10.1016/j.oceram.2021.100073.
9. Abd-Elaziem, W.; Khedr, M.; Abd-Elaziem, A.-E.; Allah, M.M.A.; Mousa, A.A.; Yehia, H.M.; Daoush, W.M.; El-Baky, M.A.A. Particle-Reinforced Polymer Matrix Composites (PMC) Fabricated by 3D Printing. J Inorg Organomet Polym 2023, 33, 3732–3749, doi:10.1007/s10904-023-02819-1.
10. Eldressi, K.A.; Alojaly, H.M.; Salem, W.O.A.; Sanoussi, N.S. Review of Recent Developments in Polymer Matrix Composites with Particulate Reinforcements. In Comprehensive Materials Processing; Elsevier, 2024; pp. 409–413 ISBN 9780323960212.
11. Díez-Pascual, A.M. Nanoparticle Reinforced Polymers. Polymers 2019, 11, 625, doi:10.3390/polym11040625.
1. Garlotta, D. A Literature Review of Poly(Lactic Acid). Journal of Polymers and the Environment 2001, 9, 63–84, doi:10.1023/A:1020200822435.
2. Singh, S.S.; Parameswaran, V.; Kitey, R. Dynamic Compression Behavior of Glass Filled Epoxy Composites: Influence of Filler Shape and Exposure to High Temperature. Composites Part B: Engineering 2019, 164, 103–115, doi:10.1016/j.compositesb.2018.11.061.
3. Bhatia, S.; Angra, S.; Khan, S. Mechanical and Wear Properties of Epoxy Matrix Composite Reinforced with Varying Ratios of Solid Glass Microspheres. J. Phys.: Conf. Ser. 2019, 1240, 012080, doi:10.1088/1742-6596/1240/1/012080.
4. Cho, J.; Joshi, M.S.; Sun, C.T. Effect of Inclusion Size on Mechanical Properties of Polymeric Composites with Micro and Nano Particles. Composites Science and Technology 2006, 66, 1941–1952, doi:10.1016/j.compscitech.2005.12.028.
5. Reuss, A. Berechnung Der Fließgrenze von Mischkristallen Auf Grund Der Plastizitätsbedingung Für Einkristalle . Z Angew Math Mech 1929, 9, 49–58, doi:10.1002/zamm.19290090104.
6. Luo, Y. Improved Voigt and Reuss Formulas with the Poisson Effect. Materials 2022, 15, 5656, doi:10.3390/ma15165656.
7. Farah, S.; Anderson, D.G.; Langer, R. Physical and Mechanical Properties of PLA, and Their Functions in Widespread Applications — A Comprehensive Review. Advanced Drug Delivery Reviews 2016, 107, 367–392, doi:10.1016/j.addr.2016.06.012.
8. Bouras, N.; Madjoubi, M.A.; Kolli, M.; Benterki, S.; Hamidouche, M. Thermal and Mechanical Characterization of Borosilicate Glass. Physics Procedia 2009, 2, 1135–1140, doi:10.1016/j.phpro.2009.11.074.
9. Abd El-Moneim, A. Quantitative Analysis of Elastic Moduli and Structure of B2O3–SiO2 and Na2O–B2O3–SiO2 Glasses. Physica B: Condensed Matter 2003, 325, 319–332, doi:10.1016/S0921-4526(02)01545-4.
10. Ohji, T. Towards Routine Tensile Testing. International Journal of High Technology Ceramics 1988, 4, 211–225, doi:10.1016/0267-3762(88)90046-X
11. Birosz, M.T.; Ledenyák, D.; Andó, M. Effect of FDM Infill Patterns on Mechanical Properties. Polymer Testing 2022, 113, 107654, doi:10.1016/j.polymertesting.2022.107654.
12. Liu, X.; Zhang, M.; Li, S.; Si, L.; Peng, J.; Hu, Y. Mechanical Property Parametric Appraisal of Fused Deposition Modeling Parts Based on the Gray Taguchi Method. Int J Adv Manuf Technol 2017, 89, 2387–2397, doi:10.1007/s00170-016-9263-3.
13. Ahn, S.; Montero, M.; Odell, D.; Roundy, S.; Wright, P.K. Anisotropic Material Properties of Fused Deposition Modeling ABS. Rapid Prototyping Journal 2002, 8, 248–257, doi:10.1108/13552540210441166.
14. Dudescu, C.; Racz, L. Effects of Raster Orientation, Infill Rate and Infill Pattern on the Mechanical Properties of 3D Printed Materials. ACTA Universitatis Cibiniensis 2017, 69, 23–30, doi:10.1515/aucts-2017-0004.
15. Alexander-Roy L, Ranaiefar M, Singh M, Halbig M. Effect of Processing Parameters on the Mechanical Behavior of 3D-Printed Basalt Moon Dust Reinforced Polylactic Acid Composites. Polymers. 2025 Oct 4;17(19):2685.

16. Alafaghani, A.; Qattawi, A.; Alrawi, B.; Guzman, A. Experimental Optimization of Fused Deposition Modelling Processing Parameters: A Design-for-Manufacturing Approach. Procedia Manufacturing 2017, 10, 791–803, doi:10.1016/j.promfg.2017.07.079.
17. D20 Committee ASTM International. Test Method for Compressive Properties of Rigid Plastics; DOI: 10.1520/D0695-23.
18. D20 Committee ASTM International. Test Method for Tensile Properties of Plastics; DOI: 10.1520/D0638-14.